Research paper

A parametric model of 3-PPR planar parallel manipulators for optimum shape design of platforms

Xiaoyong Wu [a,b], Zhijiang Xie [a], Jørgen Asbøll Kepler [b], Shaoping Bai [b,*]

[a] State Key Laboratory of Mechanical Transmission, Chongqing University, 400044 Chongqing, China
[b] Department of Mechanical and Manufacturing Engineering, Aalborg University, 9200 Aalborg, Denmark

A R T I C L E   I N F O

A B S T R A C T

This work presents a parametric model of 3-PPR[1] planar parallel manipulators, aiming to optimize shape design of the base and mobile platforms. The kinematic model is established with shape parameters and motion variables. With the model, the inverse and forward position analyses are carried out, upon which the dexterity performance in terms of conditioning index is evaluated and analyzed. The analysis of global dexterity reveals a number of platform shapes, which lead to singularity in all configurations and must be avoided in design. Further performance evaluation in terms of transmission quality is also presented. Finally, two optimal configurations for the considered manipulators are obtained from the numerical simulation results. A case study is included to demonstrate the dynamics performance with an optimal platform shape design.

© 2017 Elsevier Ltd. All rights reserved.

1. Introduction

Parallel manipulators (PMs) are closed-loop mechanisms composed of a mobile platform (MP) coupled to a fixed base by serial limbs. Compared with serial manipulators, PMs own the advantages of higher mechanical rigidity, reduced effective inertia, larger load-weight ratio, better orientation precision, suitable positional actuators arrangement and stabile capacity. On the other hand, they have some limitations, such as limited workspace, complex forward position problems and coupled dynamics, which bring challenges for the design and control of PMs [1].

Planar parallel manipulators (PPMs) are considered as a special case of PMs. They can provide planar motion with three degree of freedoms: two translations and one rotation. Extensive researches of PPMs have been reported, see e.g. [2–15]. Husty [2] studied the non-singular assembly-mode changing motions for a 3-RPR PPM. The optimum kinematic design of a 3-RRR PPM was reported in [3]. Staicu [4] focused on the inverse dynamics of a 3-PRR PPM. The kinematics performance analysis of a 3-PRP PPM called star-triangle manipulator was presented in [5]. A geometrical approach for workspace analysis of PPMs was developed in [6]. Bonev et al. [7] analyzed the singularity of PPMs through application of screw theory. Gao et al. [8] revealed the relationships between the shapes of the workspaces and the link lengths of symmetrical PPMs.

The shapes of the platforms, including the base and the MP, affect the kinematic performance of PPMs. A 3-PPR PPM has an equilateral triangle base (E-shape base) and an equilateral triangle MP (E-shape MP) was proposed by Choi et al. [9,10], for providing planar motion for a nano-scale precision manipulation. Bai and Caro introduced the 3-PPR PPM with

---

Nomenclature

l	The side length of the isosceles triangle mobile platform (MP)
l_0	The length of the bottom link of the base
l_i	The displacement of the actuating prismatic joint of limb i
θ	Half of the vertex angle of the MP
α, β	The adjacent angles of the base
x, y, ϕ	Position and orientation of the MP with respect to the global frame
$\$_{Ii}, \$_{Ti}, \$_{Oi}$	The input twist screw (ITS), transmission wrench screw (TWS) and output twist screw (OTS) of limb i
λ_i, η_i	The input and output transmission index of limb i
γ, ρ	The local and global transmission indices of the manipulator

a square base (S-shape base) and an isosceles triangle MP (I-shape MP), with the purpose to maximize its workspace [11]; error and stiffness analyses were presented in [12]. A similar 3-PPR PPM was reported by Wu et al. [13], which is a part of an assembly platform, as shown in Fig. 1. The inverse dynamics and control of the 3-PPR PPM with an S-shape base and an E-shape MP were reported in [14]. A comparison between the S-shape base and the E-shape base with respect to their workspace and kinematic sensitivity to joint clearances is available in [15].

It is noticeable that all studies above address only two special cases, i.e. E and S-shape of the base, the so called Δ and U-shape bases in literature. A more general study of 3-PPR PPMs with different shapes of the base and MP is thus needed for understanding thoroughly the kinematic and dynamic behaviors of PPMs. For this reason, this paper generalizes the shapes of the base and the MP and includes the shape parameters in the optimum design. By this approach, two optimal configurations are obtained for optimal dexterity and motion/force transmission performances. The study yields also some interesting results, namely, a number of singular shapes that are identified.

The rest of this paper is organized as follows. Section 2 contains a brief description of general 3-PPR PPMs. The inverse and forward position analyses are presented in Section 3. Performance indices in dexterity and transmission quality are described in Section 4. Performance evaluation is described in Section 5, with a case study included. Conclusions are presented in the final Section.

2. The model of general 3-PPR PPMs

A general model of the 3-PPR PPMs is proposed in this work. As shown in Fig. 2, the MP is modeled as an isosceles triangle with side length l and vertex angle 2θ, the feasible range of the angle being defined as $0° \le 2\theta \le 180°$. The base platform is defined geometrically with a segment of length l_0 of the bottom link for one linear guide and two lines with adjacent angles α, β for the other two linear guides. The feasible ranges of the angles are $0° \le \alpha \le 180°$ and $0° \le \beta \le 180°$. Some typical shapes of the base and MP are listed in Table 1.

3. Position analysis

As shown in Fig. 2, the global frame $\{O_0\}$ is attached to the base with its origin located at a vertex of the bottom side, where X_0-axis is pointed along the direction of the bottom side. Local frame $\{O\}$ is attached to the MP and defined in a similar way, with the origin located at the centroid of the MP. Moreover, the MP pose is defined by position $\mathbf{p} = [x, y]^T$ and rotation angle ϕ measured counter-clockwise from the reference point O. We assume that the initial assembly mode of the considered manipulator is defined with $\phi = 0°$.

3.1. Inverse position analysis

The inverse position problem involves mapping a known pose (position and orientation) of the MP to the actuated input of each PPR limb. In this work, the first prismatic joint in each limb is actuated, namely the considered manipulators are 3-<u>P</u>PR PPMs. For any given pose (x, y, ϕ) of the MP, the position vector of point B_i is obtained by

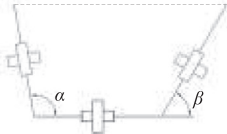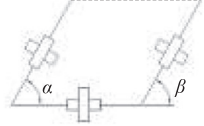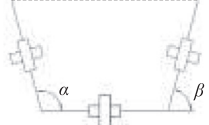$$\mathbf{b}_i = \mathbf{R}\mathbf{b}'_i + \mathbf{p}, i = 1, 2, 3 \tag{1}$$
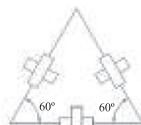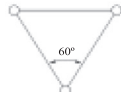
where $\mathbf{b}'_i$ is the position vector of point B_i in the local frame and $\mathbf{R}$ is the planar rotation matrix.

$$\mathbf{b}'_1 = [-a, h]^T, \mathbf{b}'_2 = [a, h]^T, \mathbf{b}'_3 = [0, -2h]^T \tag{2}$$

Here $a = l\sin\theta$ and $h = (l\cos\theta)/3$. Hence $2a$ and $3h$ define the bottom side and the height of the MP. On the other hand, the position vector of point B_i can be expressed in another form as

$$\mathbf{b}_i = \mathbf{a}_i + \mathbf{d}_i, i = 1, 2, 3 \tag{3}$$

Table 1
Typical shapes of the base and MP.

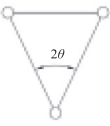| Platform	General shape description	Special shape	Range of angle	Schematic diagram
Base	T-shape (Trapezoid) $0° \leq \alpha \leq 180°$ $0° \leq \beta \leq 180°$	P-shape (Parallelogram)	$0° \leq \alpha \leq 180°$ $\beta = \alpha$	
		I-shape (Isosceles trapezoid)	$0° \leq \alpha \leq 180°$ $\beta = 180° - \alpha$	
		R-shape (Right-angle skew trapezoid)	$\alpha = 90°$ $0° \leq \beta \leq 180°$	
		S-shape (Square)	$\alpha = 90°$ $\beta = 90°$	
		E-shape (Equilateral triangle)	$\alpha = 60°$ $\beta = 120°$	
		L-shape (Line)	$\alpha = 0°, 180°$ $\beta = 0°, 180°$	
MP	I-shape (Isosceles triangle) $0° \leq \theta \leq 90°$	C-shape (Closed)	$\theta = 0°$	
		E-shape (Equilateral triangle)	$\theta = 30°$	
		O-shape (Open)	$\theta = 90°$	

where $\mathbf{a}_i$ is the position vector of point A_i, and $\mathbf{d}_i$ is the position vector of $\vec{A_iB_i}$, which are given by

$$\mathbf{a}_1 = l_1\mathbf{e}_1, \mathbf{a}_2 = l_0\mathbf{e}_3 + l_2\mathbf{e}_2, \mathbf{a}_3 = l_3\mathbf{e}_3, \mathbf{d}_1 = d_1\mathbf{n}_1, \mathbf{d}_2 = d_2\mathbf{n}_2, \mathbf{d}_3 = d_3\mathbf{n}_3 \qquad (4)$$

where l_i is the displacement of the ith $\underline{P}$ joint, d_i is the distance between point A_i and B_i, while $\mathbf{e}_i$ and $\mathbf{n}_i$ are unit vectors parallel to the translation direction of corresponding prismatic joints.
Eqs. (1) and (3) yield

$$\mathbf{b}_i = \mathbf{R}\mathbf{b}'_i + \mathbf{p} = \mathbf{a}_i + \mathbf{d}_i, i = 1, 2, 3 \qquad (5)$$
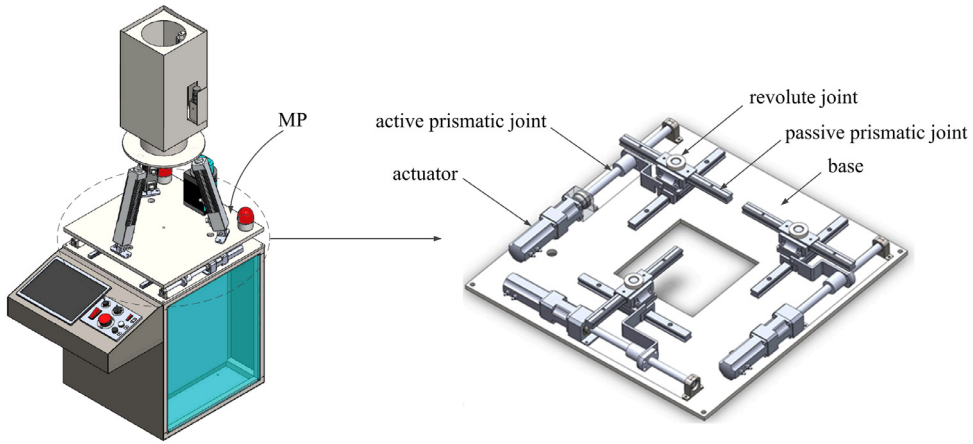
Fig. 1. CAD model of an assembly platform for optical modules assembling in a laser lab, in which the platform uses a 3-PPR PPM to provide planar motion for the positioning device on the top.
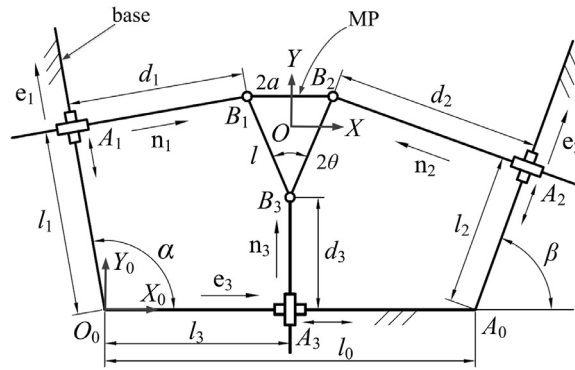

Fig. 2. Schematic diagram of general 3-PPR PPMs.

Expanding Eq. (5) leads to

$$
\begin{cases}
l_1 = x\cos\alpha + y\sin\alpha - h\sin(\phi-\alpha) - a\cos(\phi-\alpha) & \text{(6a)}\\
l_2 = (x-l_0)\cos\beta + y\sin\beta + a\cos(\phi-\beta) - h\sin(\phi-\beta) & \text{(6b)}\\
l_3 = x + 2h\sin\phi & \text{(6c)}\\
d_1 = x\sin\alpha - y\cos\alpha + a\sin(\phi-\alpha) - h\cos(\phi-\alpha) & \text{(6d)}\\
d_2 = (l_0-x)\sin\beta + y\cos\beta + h\cos(\phi-\beta) + a\sin(\phi-\beta) & \text{(6e)}\\
d_3 = y - 2h\cos\phi & \text{(6f)}
\end{cases}
$$

Since the first P joint in each limb is actuated, the inverse position problem of the considered 3-$\underline{P}$PR PPMs is to determine the actuated inputs l_i, and they can be directly determined from Eqs. (6a) to (6c). On the other hand, Eqs. (6d)–(6f) will give the solutions to the inverse position problem if the second P joint in each limb is chosen as the actuated joint.

Differentiating both sides of Eqs. (6a)–(6c) with respect to time, we obtain

$$\dot{\mathbf{u}} = \mathbf{J}^{-1}\dot{\mathbf{x}} \tag{7}$$

where $\dot{\mathbf{u}} = [\dot{l}_1, \dot{l}_2, \dot{l}_3]^T$ is the velocity vector of the $\underline{P}$ joints, $\dot{\mathbf{x}} = [\dot{x}, \dot{y}, \dot{\phi}]^T$ is the velocity vector of the MP. $\mathbf{J}^{-1}$ is the inverse Jacobian matrix, which is

$$\mathbf{J}^{-1} = \begin{bmatrix} \cos\alpha & \sin\alpha & a\sin(\phi-\alpha) - h\cos(\phi-\alpha) \\ \cos\beta & \sin\beta & -a\sin(\phi-\beta) - h\cos(\phi-\beta) \\ 1 & 0 & 2h\cos\phi \end{bmatrix} \tag{8}$$

3.2. Forward position analysis

In the forward position problem of the 3-$\underline{P}$PR PPMs, the pose of the MP is to be found for any given inputs of the $\underline{P}$ joints. By virtue of Eqs. (6a) and (6c), we can get the solutions of x and y expressed by ϕ

$$\begin{cases} x = l_3 - 2h\sin\phi & \text{(9a)} \\ y = \frac{1}{\sin\alpha}(l_1 - (l_3 - 2h\sin\phi)\cos\alpha + h\sin(\phi - \alpha) + a\cos(\phi - \alpha)) & \text{(9b)} \end{cases}$$

Substituting Eqs. (9a) and (9b) into Eq. (6b) leads to

$$M\sin\phi + N\cos\phi + Q = 0 \tag{10a}$$

where

$$\begin{cases} M = 2a\sin\beta - 3h\cos\beta + 3h\sin\beta\cot\alpha \\ N = a\cos\beta + a\sin\beta\cot\alpha \\ Q = \frac{\sin\beta}{\sin\alpha}(l_1 - l_3\cos\alpha) + (l_3 - l_0)\cos\beta - l_2 \end{cases} \tag{10b}$$

When $\sin\alpha = 0$ ($\alpha = 0°$ or $180°$) we have

$$y = a\sin\phi - h\cos\phi - l_2, \ M = 3h, \ N = a, \ Q = l_1 - l_3 \tag{11}$$

Then we can get the solution of ϕ

$$\phi = \tan^{-1}\left(\frac{M}{N}\right) \pm \cos^{-1}\left(\frac{-Q}{\sqrt{M^2 + N^2}}\right) \tag{12}$$

Obviously, the solutions of forward position problem can be derived from Eqs. (9a), (9b) and (12), but the Jacobian matrix **J** cannot be obtained directly from these equations. Here, we can resort to Eq. (8), the inverse matrix of $\mathbf{J}^{-1}$ will give the answer to the Jacobian matrix by numerical method.

4. Performance indices

In the optimum design, two performance indices, one for the kinematic performance, and the other for the transmission quality, are considered.

4.1. Dexterity index

Dexterity index is defined as a measure to evaluate the ability of a manipulator to arbitrarily change its pose. It depends on the structure of the manipulator, and it can be expressed in terms of the properties of Jacobian matrix.

Several indices have been proposed to measure manipulator dexterity, see e.g. [16–19]. One of the frequently used indices is called conditioning index which based on condition number as introduced in [16]. The condition number is applied to evaluate the velocity, rigidity and accuracy mapping characteristics between the MP and the joint variables [17]. The condition number of a Jacobian matrix of full rank can be defined as

$$k = \|\mathbf{J}\| \left\|\mathbf{J}^{-1}\right\| \tag{13}$$

where $\|\bullet\|$ denotes the matrix norm, and the usually used matrix norm is Frobenius norm. Since the condition number does not have an upper bound, its reciprocal known as local conditioning index (LCI) is more frequently used [18].

$$\text{LCI} = \frac{1}{k} \tag{14}$$

LCI is bounded in the range of 0 to 1, where 0 represents the singularity poses and 1 denotes the isotropic configuration. Therefore, the higher the value of LCI, the greater the dexterity of the manipulator is. Obviously, LCI depends on the joints coordinates which means it is pose-dependent, and it is applied to evaluate the local dexterity.

In order to evaluate the global dexterity of the manipulator over the entire workspace, Gosselin [19] proposed the global conditioning index (GCI) as

$$\text{GCI} = \frac{\int_W \left(\frac{1}{k}\right) dW}{\int_W dW} \tag{15}$$

where W is the point distributed in the workspace, and GCI denotes the average value of $1/k$ over the workspace. Considering the shape complexity of the workspace, the GCI is normally calculated numerically as

$$\text{GCI} \approx \frac{1}{N_W} \sum_{j=1}^{N_W} \frac{1}{k} \tag{16}$$

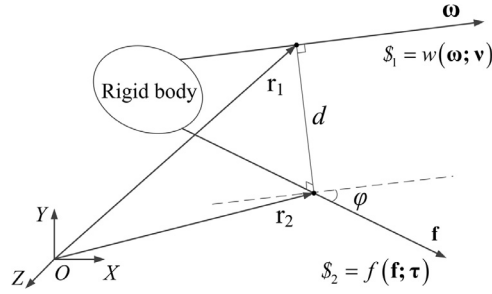where N_W is equal to the number of the points uniformly distributed over the workspace.

Fig. 3. The twist and wrench screws of a rigid body.

4.2. Motion/force transmission index

In this work, transmission quality evaluation based on screw theory is adopted. The general definition of motion/force transmission index is first introduced, upon which the index for the PPMs is derived.

4.2.1. Definitions of motion/force transmission index

As depicted in Fig. 3, a twist screw can be used to represent the instantaneous motion of a rigid body

$$\$_1 = w(\boldsymbol{\omega}; \boldsymbol{v}) = w(\boldsymbol{\omega}; \mathbf{r}_1 \times \boldsymbol{\omega} + h_1\boldsymbol{\omega}) = (L_1, M_1, N_1; \ P_1, Q_1, R_1) \tag{17}$$

where $\boldsymbol{\omega}$ is the unit rotational velocity of the rigid body, $\mathbf{r}_1$ is the position vector of a point on the twist axis, w represents the amplitude of the twist screw, and h_1 defines the pitch. Similarly, a wrench screw can express the wrench exerted on the rigid body

$$\$_2 = f(\mathbf{f}; \tau) = f(\mathbf{f}; \mathbf{r}_2 \times \mathbf{f} + h_2\mathbf{f}) = (L_2, M_2, N_2; P_2, Q_2, R_2) \tag{18}$$

where $\mathbf{f}$ represents the unit pure force vector, $\mathbf{r}_2$ is the position vector of a point on the wrench axis, f denotes the amplitude of the wrench screw, and h_2 defines the pitch.

The reciprocal product between twist screw $\$_1$ and wrench screw $\$_2$ is defined as

$$\$_1 \circ \$_2 = L_1 P_2 + M_1 Q_2 + N_1 R_2 + L_2 P_1 + M_2 Q_1 + N_2 R_1 = (h_1 + h_2)\cos\varphi - d\sin\varphi \tag{19}$$

where φ and d are the angle and distance between these two screws. It can be seen that the reciprocal product indicates their instantaneous power [20], and the wrench will not apply any work to the rigid body if the reciprocal product is equal to 0. Transmission quality can be defined by the twist and wrench screws as [21],

$$TI = \frac{\$_1 \circ \$_2}{|\$_1 \circ \$_2|_{max}} = \frac{|(h_1 + h_2)\cos\varphi - d\sin\varphi|}{\sqrt{(h_1 + h_2)^2 + d_{max}^2}} \tag{20}$$

where d_{max} is the potential maximal distance between the two screws.

Considering the two screws in one limb, namely, $\$_{Ii}$, the input twist screw (ITS) and $\$_{Ti}$, the transmission wrench screw (TWS), transmission quality at the input side called input transmission index (ITI) is defined as

$$\lambda_i = \frac{\$_{Ii} \circ \$_{Ti}}{|\$_{Ii} \circ \$_{Ti}|_{max}} \tag{21}$$

The transmission quality at the output side, called output transmission index (OTI), is defined as

$$\eta_i = \frac{\$_{Oi} \circ \$_{Ti}}{|\$_{Oi} \circ \$_{Ti}|_{max}} \tag{22}$$

where $\$_{Oi}$ is the output twist screw (OTS), which represents the instantaneous motion of the moving platform when fixing all the actuators except the one in the ith limb [22].

On the basis of ITI and OTI, the local transmission index (LTI) of a PM with n-DOF is defined as

$$\gamma = \min(\min(\lambda_i), \min(\eta_i)), (i = 1, 2, \cdots, n) \tag{23}$$

In order to obtain high quality of force/motion transmissibility, the most widely accepted design limit for the transmission angle is [45°, 135°]. According to literature [20,23], the LTI should be no smaller than $\sin 45° \approx 0.7$. The set of poses is called the good transmission workspace (GTW) when $\gamma \geq 0.7$.

As our interest is the overall performance of PMs, we introduce global transmission index (GTI), in analogy to GCI, which is calculated numerically as

$$\rho \approx \frac{1}{N_W} \sum_{j=1}^{N_W} \gamma \tag{24}$$

GTI ranges from 0 to 1, the larger the value of GTI, the better the global transmission performance.
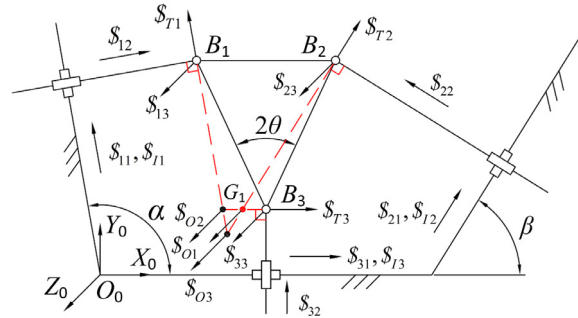
Fig. 4. Screw system in the 3-PPR PPMs.

4.2.2. Motion/force transmission index of 3-PPR PPMs

As shown in Fig. 4, the considered PPMs can be expressed by screws. Taking the first PPR limb for an example, with respect to the global frame, the twist screws can be written as

$$
\begin{cases}
\$_{11} = (0, 0, 0;\ \cos\alpha, \sin\alpha, 0) \\
\$_{12} = (0, 0, 0;\ \sin\alpha, -\cos\alpha, 0) \\
\$_{13} = \left(0, 0, 1;\ b_{1y}, -b_{1x}, 0\right)
\end{cases}
\tag{25}
$$

where b_{ix} and b_{iy} ($i = 1, 2, 3$) are the coordinates of point B_i, which can be solved from Eq. (3). $U_1^k = \{\$_{11}, \$_{12}, \$_{13}\}$ represents the kinematic screw system of the first limb. Since the first prismatic joint is active, the corresponding twist screw is the ITS

$$
\$_{I1} = \$_{11} = (0, 0, 0;\ \cos\alpha, \sin\alpha, 0)
\tag{26}
$$

In a similar way, two other ITSs of the considered 3-PPR PPMs can be derived as

$$
\$_{I2} = \$_{21} = (0, 0, 0;\ \cos\beta, \sin\beta, 0)
\tag{27}
$$

$$
\$_{I3} = \$_{31} = (0, 0, 0;\ 1, 0, 0)
\tag{28}
$$

Three linearly independent screws which are reciprocal to U_1^k are obtained

$$
\begin{cases}
\$_{11}^r = (0, 0, 1;\ 0, 0, 0) \\
\$_{12}^r = (0, 0, 0;\ 1, 0, 0) \\
\$_{13}^r = (0, 0, 0;\ 0, 1, 0)
\end{cases}
\tag{29}
$$

where $\$_{1i}^r$ ($i = 1, 2, 3$) is the constraint wrench screw that the PPR limb provides for the MP, and $U_c = \{\$_{11}^r, \$_{12}^r, \$_{13}^r\}$ denotes the constraint wrench screw system. Moreover, all the three PPR limbs provide the same constraint wrench screw system.

As for the TWS of the first PPR limb, it is reciprocal to all the passive joint screws in U_1^k ($\$_{12}$ and $\$_{13}$). In addition, all the wrench screws in U_c are linear independent, and we have

$$
\$_{T1} = \left(\cos\alpha, \sin\alpha, 0;\ 0, 0, b_{1x}\sin\alpha - b_{1y}\cos\alpha\right)
\tag{30}
$$

It is a pure force parallel to the moving direction of the P joint in the first limb, and passes through point B_1, as shown in Fig. 4. The TWSs of the second and third limbs can be obtained by the same approach,

$$
\$_{T2} = \left(\cos\beta, \sin\beta, 0;\ 0, 0, b_{2x}\sin\beta - b_{2y}\cos\beta\right)
\tag{31}
$$

$$
\$_{T3} = \left(1, 0, 0;\ 0, 0, -b_{3y}\right)
\tag{32}
$$

From above equations, it can be obtained that

$$
\$_{Ii} \circ \$_{Ti} = 1,\ i = 1, 2, 3
\tag{33}
$$

Obviously, the corresponding twist and wrench are parallel to each other, which means the motion from the actuator can be totally transmitted by its transmission wrench, and it leads to

$$
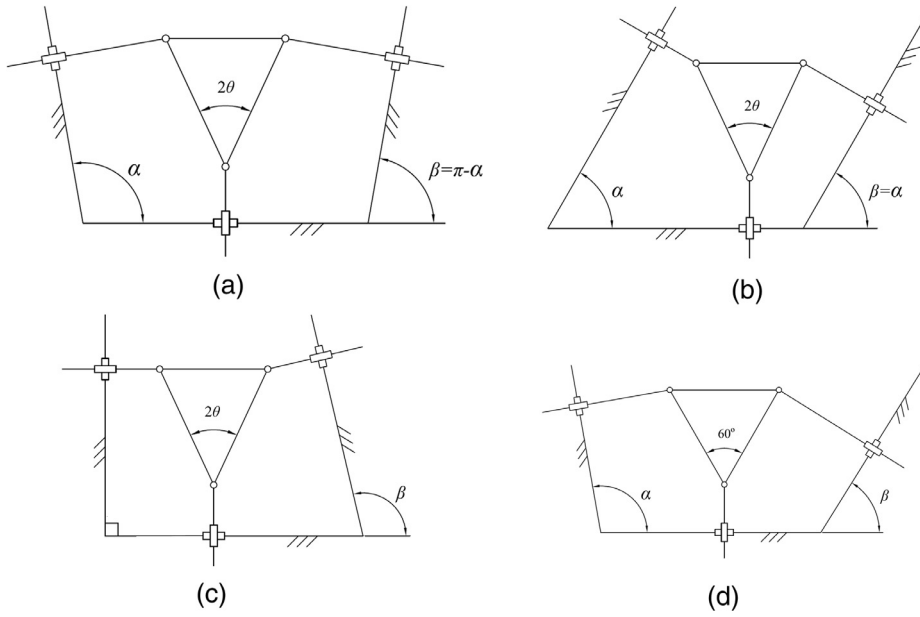\lambda_i = \frac{\$_{Ii} \circ \$_{Ti}}{|\$_{Ii} \circ \$_{Ti}|_{\max}} = 1,\ i = 1, 2, 3
\tag{34}
$$

Fig. 5. Typical shapes of 3-$\underline{P}$PR PPM platforms: (a) I-I, (b) P-I, (c) R-I and (d) T-E shape.

We can now determine the OTS of each limb. Taking the first limb for an example, as $\$_{O1}$ is reciprocal to $\{\$^r_{11}, \$^r_{12}, \$^r_{13}, \$_{T2}, \$_{T3}\}$, we thus have

$$\$_{O1} = \begin{cases} (0, 0, 1; b_{3y}, b_{2y}\cot\beta - b_{3y}\cot\beta - b_{2x}, 0), 0° < \beta < 180° \\ (0, 0, 1; 0, 1, 0), \text{others} \end{cases} \tag{35}$$

As can be seen in the equation, when $0° < \beta < 180°$, $\$_{O1}$ is a pure rotation, the axis of which being perpendicular to the plane $B_1B_2B_3$ and passing through point G_1, where G_1 is the center of rotation when the second and third $\underline{P}$ joints are locked, as shown in Fig. 4. When $\beta = 0°$ or $180°$, $\$_{O1}$ is a pure translation, which is parallel to the Y_0-axis.

By the same approach, we can get the OTSs for another two limbs

$$\$_{O2} = \begin{cases} (0, 0, 1; b_{3y}, b_{1y}\cot\alpha - b_{3y}\cot\alpha - b_{1x}, 0), 0° < \alpha < 180° \\ (0, 0, 1; 0, 1, 0), \text{others} \end{cases} \tag{36}$$

$$\$_{O3} = (0, 0, 1; Q_1, Q_2, 0) \tag{37}$$

where

$$\begin{cases} Q_1 = \dfrac{b_{1y}\sin\beta\cos\alpha - b_{2y}\sin\alpha\cos\beta + (b_{2x} - b_{1x})\sin\alpha\sin\beta}{\sin(\beta - \alpha)} \\ Q_2 = \dfrac{b_{2x}\sin\beta\cos\alpha - b_{1x}\sin\alpha\cos\beta + (b_{1y} - b_{2y})\cos\alpha\cos\beta}{\sin(\alpha - \beta)} \end{cases} \tag{38}$$

for cases $\sin(\alpha\text{-}\beta) \neq 0$.

When $\sin(\alpha\text{-}\beta) = 0$, two cases are implied. The first case is that PPMs are designed with the L-I shape platforms, as shown in Fig. 9(a). In such a case, the MP can only translate perpendicular to the moving direction of the third $\underline{P}$ joint, if the actuators in the first and second limbs are fixed. This means that the OTS of the third limb is a pure translation normal to moving direction of the $\underline{P}$ joint in the third limb. At the meantime, the TWS of the third limb is a pure force parallel to the moving direction of the third $\underline{P}$ joint as discussed above. Therefore, the twist and wrench are orthogonal, and the third limb does not make any contribution to balance the load exerted on the MP. As a result, all the OTIs of the three limbs within the L-I shape are equal to 0, hence the LTI is 0.

In the second case, PPMs have platforms of the P-I shape, as shown in Fig. 5(b). If the $\underline{P}$ joints in the first and second limbs are fixed, the MP could only translate along the moving direction of the P joint in the first (second) limb, which means the OTS of the third limb is a pure translation, and we have

$$\$_{O3} = (0, 0, 0; \sin\alpha, -\cos\alpha, 0) \tag{39}$$

Since $\lambda_i = 1$, the LTI of the considered 3-$\underline{P}$PR PPMs can be calculated based on following equation

$$\gamma = \min(\eta_i) = \min\left(\frac{\$_{Oi} \circ \$_{Ti}}{|\$_{Oi} \circ \$_{Ti}|_{\max}}\right), i = 1, 2, 3 \tag{40}$$
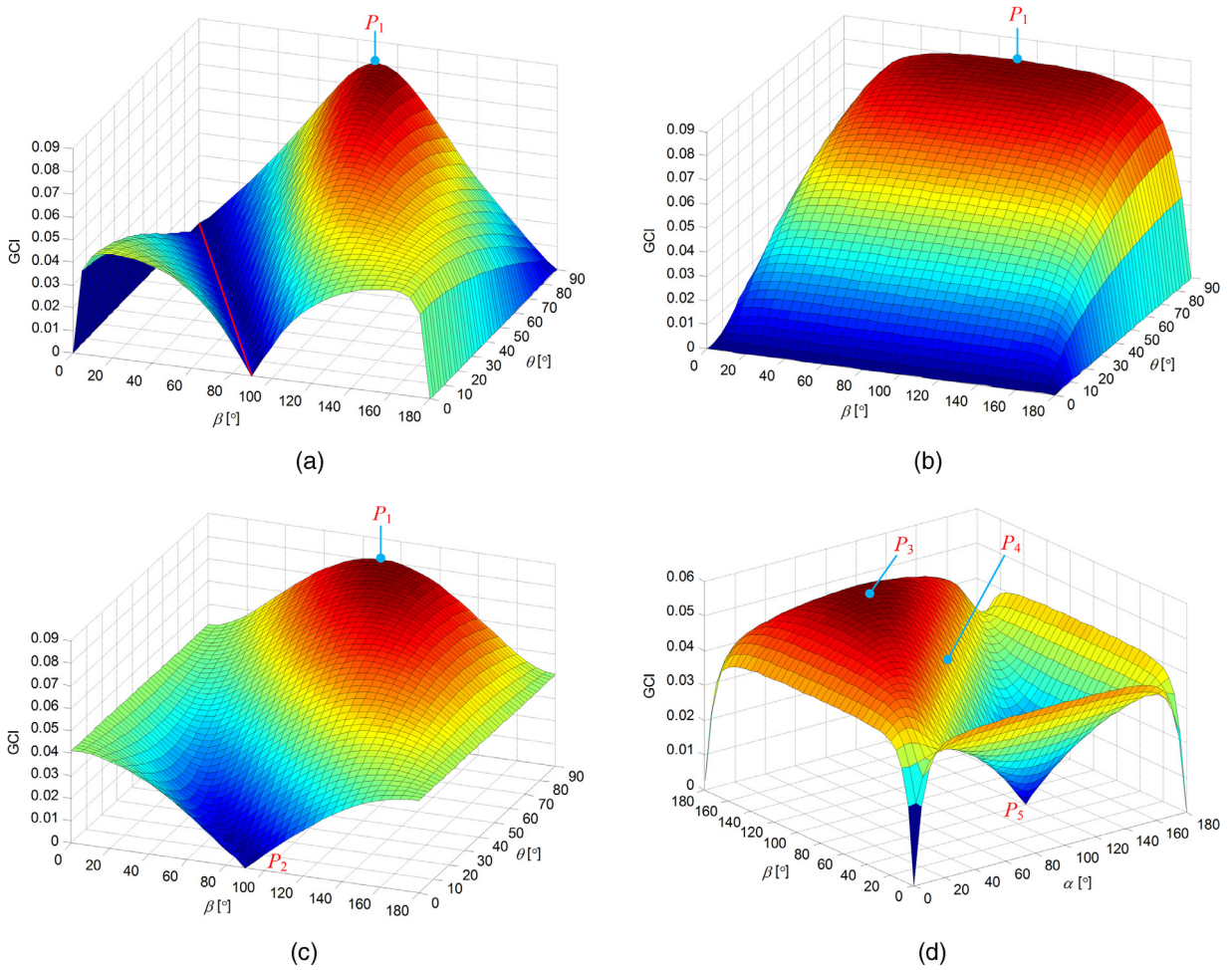
Fig. 6. GCI of PPMs with platforms of (a) I-I, (b) P-I, (c) R-I and (d) T-E shape.

5. Performance evaluation

With the selected performance indices, optimum platform design is conducted. We look at first on the optimum kinematic design. Afterwards, the optimum design in terms of transmission quality is considered.

5.1. Dexterity performance evaluation

Four typical shapes, as shown in Fig. 5, are taken into consideration. They include the I-I, P-I, R-I and T-E shapes, where the first and the second letters represent the shapes of the base and the MP, as defined in Table 1. In particular, the first three shapes have an isosceles triangle MP, while their bases are designed as isosceles trapezoid ($\alpha + \beta = 180°$), parallelogram ($\beta = \alpha$) and right-angle skew trapezoid ($\alpha = 90°$), respectively. The T-E shape PPM has an equilateral triangle MP, with a trapezoid base ($0° \leq \alpha,\ \beta \leq 180°$). As reported in [10], the 3-PPR PPM under study will obtain great global performance when $l /l_0 = 0.5$. For this reason, the dimensional parameters of the considered PPMs in this work are taken as $l_0 = 0.32$ m, $l = 0.16$ m.

The GCIs of PPMs associated to the four typical shapes are depicted in Fig. 6. It is seen that the I-I, P-I, and R-I shapes have the same maximum GCI, which is equal to 0.0808, as the point P_1 in the plots. The optimal shape is shown in Fig. 7, which corresponds to $\alpha = \beta = 90°$ and $\theta = 90°$, or S-O shape, which means that the isosceles triangle MP is opened and transformed to a line.

For the T-E shape, as shown Fig. 6(d), the maximum GCI is found as 0.0581, as the point P_3 in the plot. This corresponds to the E-E shape platforms. In the plot, point P_4 stands for the S-E shape platforms, for which the GCI is equal to 0.0410.

Fig. 8 shows the contour map of the GCI of PPMs with the P-I shape platforms. It can be observed that the GCI is symmetrically distributed about $\beta = 90°$.
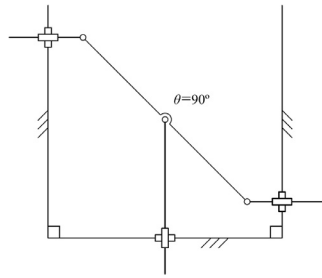
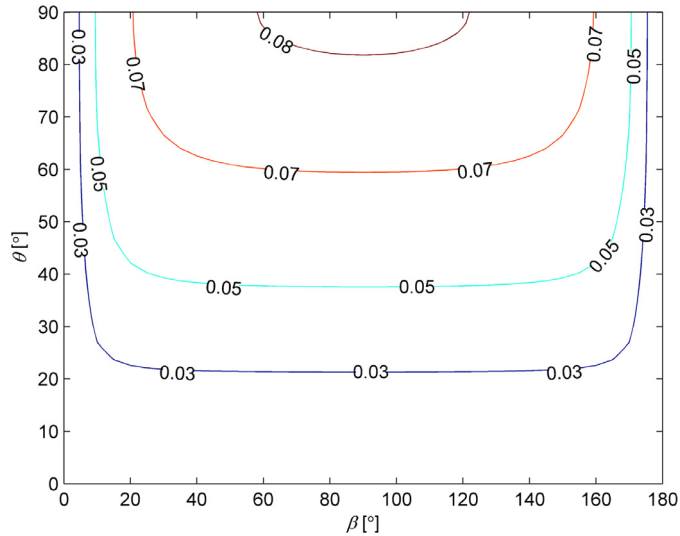**Fig. 7.** A PPM with S-O shape platforms has the maximum GCI. Three R joints are located on one line.

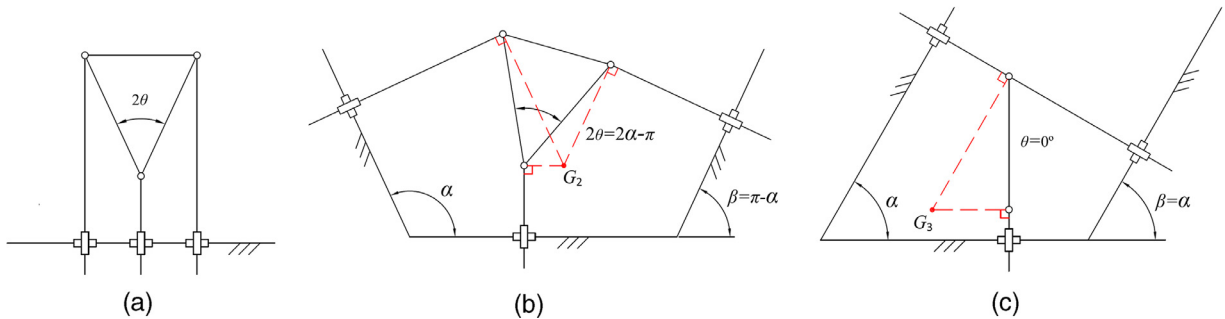**Fig. 8.** Contour map of GCI of a PPM with the P-I shape platforms.

Fig. 9. 3-$\underline{P}$PR PPMs with (a) L-I, (b) I=I and (c) P-C shape platforms are always singular. In the figure, G_2 and G_3 are instantaneous centers of rotation.

It is noticeable that the GCI is equal to 0 in a few cases. A zero GCI implies zero LCI in all configurations. In other words, the PPM is always singular, to which we refer as *shape singularity* to distinguish from other types of singularities. These cases include the followings:

- L-I shape platforms. In Fig. 6(a), the GCI is equal to 0 in case of ($\alpha = 0°$, $\beta = 180°$) and ($\alpha = 180°$, $\beta = 0°$) with the I-I shape, these two cases pertain to the L-I shape, as shown in Fig. 9(a), where the three $\underline{P}$PR limbs are parallel to each other. With this shape, the MP can still move along the direction of the P joints even without actuating the three $\underline{P}$ joints.
  In Fig. 6(b), the singular shapes are also found for ($\alpha = 0°$, $\beta = 0°$) and ($\alpha = 180°$, $\beta = 180°$) with the P-I shape, which also correspond to the L-I singular shape. Moreover, the four PPMs represented by the four corner points in Fig. 6(d) pertain to the L-I singular shape as well.
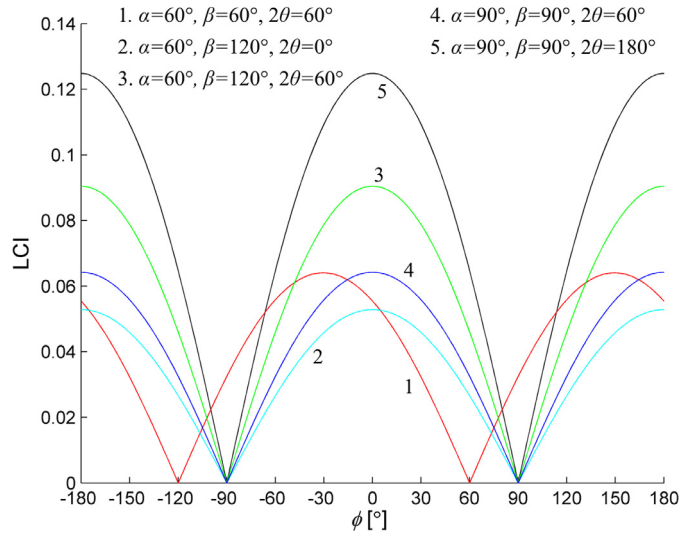
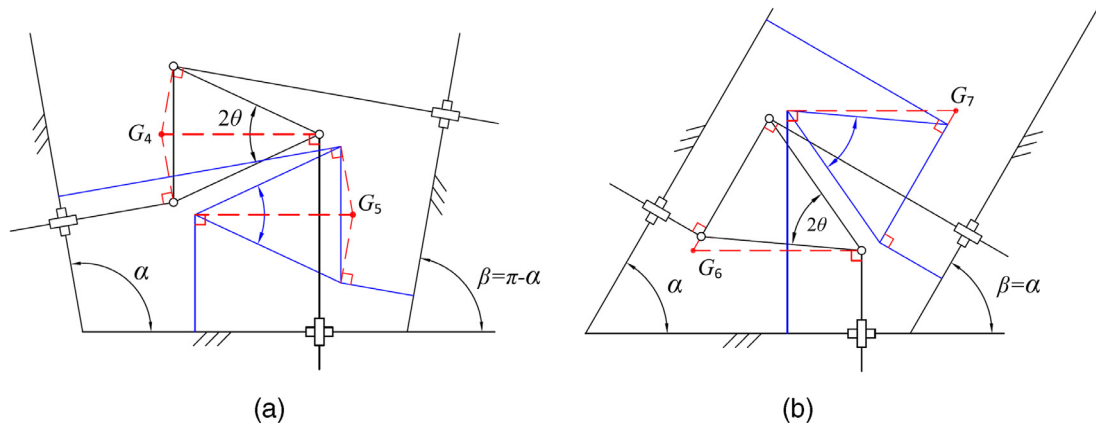**Fig. 10.** LCI of the 3-PPR PPMs with different platform shapes.

Fig. 11. Singularity configurations of 3-PPR PPMs with platforms of (a) I-I ($\alpha + \beta = 180°$) and (b) P-I ($\beta = \alpha$) shape.

- I=I shape platforms. In Fig. 6(a), there is a red line where the GCI is equal to 0. The PPMs on this line are defined by $\alpha + \beta = 180°$, $2\theta = 2\alpha - 180°$, and $\alpha > 90°$, where the base is an isosceles trapezoid. As the intersection angle made by the first and second P joint axes is equal to 2θ too, we note the shapes of the base and the MP by 'I=I'. For PPMs constructed with this type of platform shape, the MP can still perform a small rotation about a specific point even all the actuators are locked, as depicted in Fig. 9(b).
  Noted that, the PPM platform represented by point P_5 ($\alpha = 120°$, $\beta = 60°$, $\theta = 30°$) in Fig. 6(d) is a special case of the I=I singular shape.

- P-C shape platforms. In Fig. 6(b), singular shape is identified with the P-C shape ($\beta = \alpha$, $\theta = 0°$). This singular shape is shown in Fig. 9(c). The MP can still perform a small rotation about the instantaneous center of rotation (G_3) even without actuating all the three actuators. The singular shape identified at point P_2 ($\beta = \alpha = 90°$, $\theta = 0°$) in Fig. 6(c) corresponds to the P-C singular shape too.

In this work, we also look further into the local dexterity performance, selecting five different designs of the considered 3-PPR PPMs. These cases are PPMs of (1) P-I shape, (2) E-C shape, (3) E-E shape, (4) S-E shape, and (5) S-O shape.

Fig. 10 shows LCIs with 5 PPMs rotating for 360°. As shown in the figure, the S-O shape (case 5) also possesses the best local dexterity and its maximum LCI is 0.1248. Within E-C (case 2), E-E (case 3), S-E (case 4) and S-O shapes, the manipulator will reach singularities in cases of $\phi = \pm 90°$ where the LCI is equal to 0. The singularity is demonstrated in Fig. 11(a), where G_4 and G_5 are the instantaneous centers of rotation even locking all the actuators. For Case 1 ($\beta = \alpha = 60°$, $\theta = 30°$), singularities are found with $\phi = 60°$ and $-120°$, this configuration corresponds to the P-I shape, and it can be
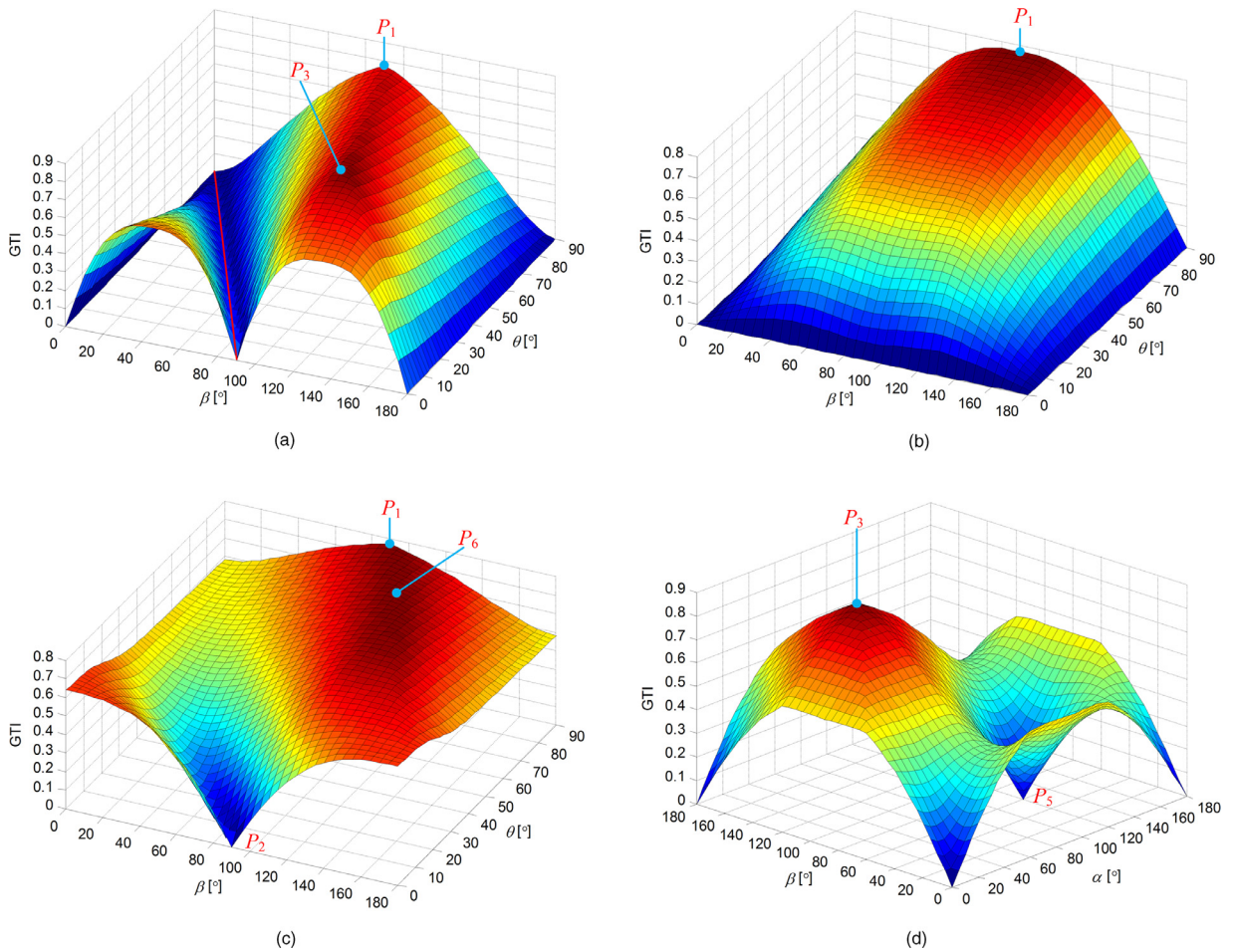
Fig. 12. GTI of PPMs with MP platforms of (a) I-I, (b) P-I, (c) R-I and (d) T-E shape.

observed that $\phi = \alpha$ and $\alpha - 180°$ are the singularities for general P-I shape, as demonstrated in Fig. 11(b), where G_6 and G_7 are the instantaneous centers of rotation.

5.2. Motion/force transmission evaluation

The four platform shapes as discussed in Section 5.1 are considered. Their GTI distributions are depicted in Fig. 12. Comparing Figs. 6 and 12, it is found that the distributions of GCI and GTI within corresponding shapes are very similar, while some differences are noticeable.

It is seen in both Figs. 12(a) and (d) that the maximum GTI is equal to 0.8314 at point P_3 in the two plots. The corresponding PPM platforms are of E-E shape. In Fig. 12(b), the maximum GTI is equal to 0.7701 at point P_1, which corresponds to S-O shape. The maximum GTI in Fig. 12(c) is equal to 0.7720 at point P_6 ($\alpha = 90°$, $\beta = 112°$, $\theta = 68°$).

It is noticeable that the GTI indicates the same singular shapes as the GCI, namely, the L-I, I=I and P-C singular shapes. As analyzed in Section 4.2.2, the LTI of the L-I shape is always equal to 0, so it is a singular shape. For the I=I and P-C shapes, as shown in Fig. 13(a) and (b), $\$_{T1}$ and $\$_{O1}$ intersect vertically, their reciprocal product is equal to 0, so does the GTI. In light of this, the singular shapes can also be identified from GTI plot in Fig. 12.

Fig. 14 shows the LTI distribution of the same five chosen designs as mentioned in the analysis of LCI. The PPM of E-E shape also owns the best local transmission quality. Its LTI is equal to 0 when $\phi = \pm 90°$, which is also the configurations of singularity. The GTW workspace is found with ϕ in the range of $[-72°, 72°]$. The manipulator has the best force/motion transmissibility when $\phi = 0°$.

In summary, dexterity and transmissibility show their similarities in the distribution over shape design parameters. Both GCI and GTI can be applied to determine the singular shapes, while LCI and LTI are useful to solve the singularities of different configurations. On the other hand, there are also some differences in the two performance indices, as analyzed in
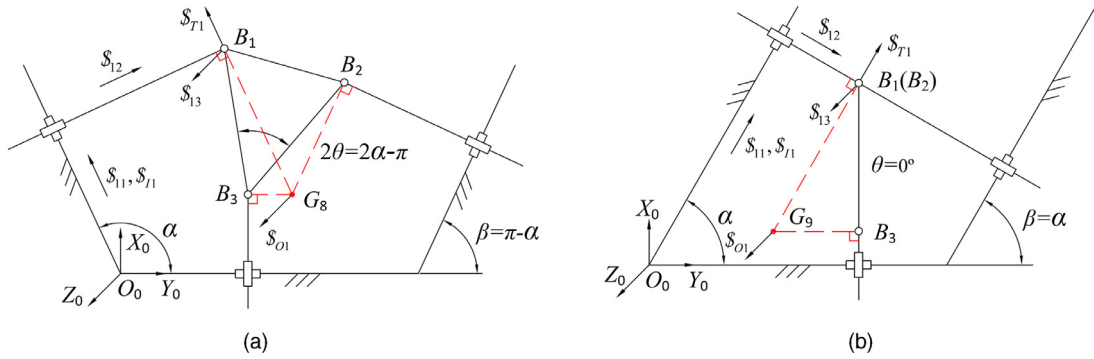
Fig. 13. The first PPR limb expressed by screws within (a) I=I and (b) P-C shape.
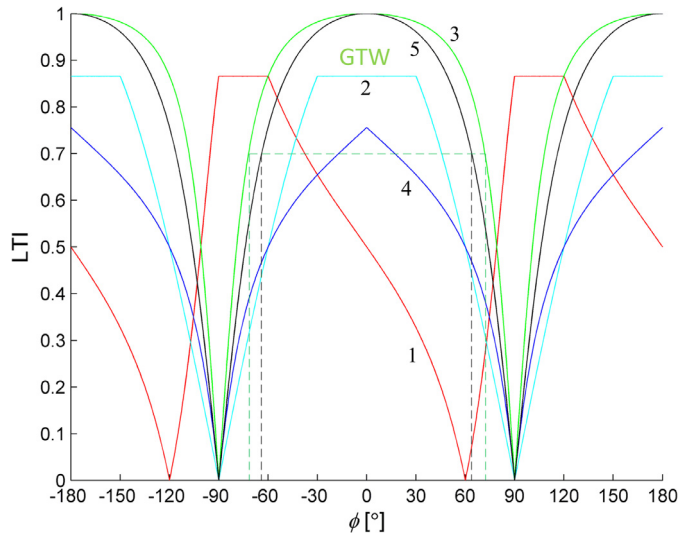

Fig. 14. LTI of the 3-PPR PPMs with five designs of platforms.

Table 2
Optimal and singular shapes of the 3-PPR PPMs.

Platform		I-I	P-I	R-I	T-E
Optimal shapes	GCI	S-O	S-O	S-O	E-E
	GTI	E-E	S-O	$\beta = 112°$, $\theta = 68°$	E-E
Singular shapes	GCI	$\beta = 0°$; $\beta = 180°$; $\theta = \alpha - 90°$	$\beta = 0°$; $\beta = 180°$; $\theta = 0°$	$\beta = 90°$, $\theta = 0°$	$\alpha = 0°$, $\beta = 0°$; $\alpha = 0°$, $\beta = 180°$; $\alpha = 120°$, $\beta = 60°$; $\alpha = 180°$, $\beta = 0°$; $\alpha = 180°$, $\beta = 180°$
	GTI	$\beta = 0°$; $\beta = 180°$; $\theta = \alpha - 90°$	$\beta = 0°$; $\beta = 180°$; $\theta = 0°$	$\beta = 90°$, $\theta = 0°$	$\alpha = 0°$, $\beta = 0°$; $\alpha = 0°$, $\beta = 180°$; $\alpha = 120°$, $\beta = 60°$; $\alpha = 180°$, $\beta = 0°$; $\alpha = 180°$, $\beta = 180°$

this section. The PPMs of S-O shape show the best dexterity, while PPMs of E-E shape have the best transmission quality. The optimal and singular shapes of the four discussed typical platforms in terms of dexterity and transmission quality are summarized in Table 2.

5.3. A case study of dynamic performance with the optimum platform shape design

We include a case study of dynamics simulation to show the dynamic behavior of the optimum design. The masses are taken as $m_1 = 1.7574$ kg, $m_2 = 0.8313$ kg, $m_3 = 48.4972$ kg, where m_1, m_2 and m_3 stand for the masses of the driving part, passive part and MP, respectively. The corresponding moments of inertia are taken as $I_1 = 0.0043$ kg m^2, $I_2 = 0.0039$ kg m^2 and $I_3 = 2.9431$ kg m^2.
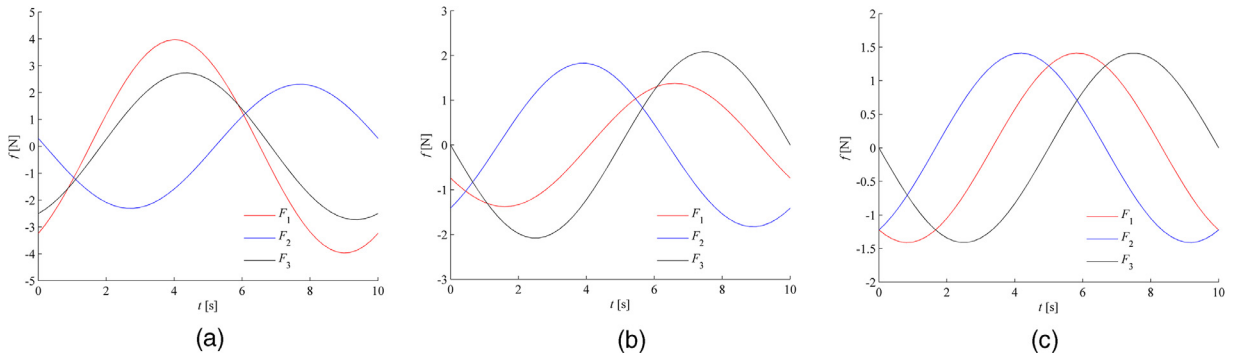
Fig. 15. Simulation of driving forces for PPMs with platforms of (a) a general shape, (b) the S-O shape and (c) the E-E shape.

The trajectory of the MP is defined as

$$
\begin{cases}
x = \frac{1}{2}l_0 + \frac{1}{10}\sin\left(\frac{\pi}{5}t\right) \\
y = \frac{\sqrt{3}}{4}l_0 + \frac{1}{10}\cos\left(\frac{\pi}{5}t\right) \\
\phi = \frac{\pi}{6}
\end{cases}
\tag{41}
$$

Three designs including a general platform shape ($\alpha = 135°$, $\beta = 45°$, $\theta = 30°$) and the two optimum designs (S-O and E-E shapes) are considered, while the dimensional parameters are the same as given in Section 5.1. The driving forces can be readily obtained, and the results of this given motion are shown in Fig. 15, where F_i is the driving force of limb i.

The maximum driving forces for the three designs with the given motion trajectory are 3.97 N, 2.08 N, and 1.41 N, respectively. Obviously, the optimum PPMs of E-E shape and S-O shape show performance improvement over the PPM of general shape platforms. Moreover, the PPM of E-E shape has the better force/motion transmission quality than the PPM of S-O shape, if we evaluate in terms of the magnitude of required driving forces. The result is in line with the analysis that PPMs of E-E shape has the best transmission quality.

6. Discussion and conclusions

In this work, a parametric model with shape parameters and motion variables is established, aiming to optimize shape of the base and MP of general 3-PPR PPMs. In the optimum shape design, the dexterity and motion/force transmission performances are considered. The study shows that the PPMs of S-O shape exhibit the best dexterity, while PPMs of the E-E shape show the best transmission quality. A case study of dynamics simulation is included to demonstrate the dynamic behavior of the PPMs of E-E shape.

A contribution of this work is the establishment of a parametric model of 3-PPR PPMs. By including the shape parameters of the base and mobile platforms, the model allows us to investigate the influence of the platforms' shape on the kinematic and dynamic performances. The optimal shape design in this work shows the significance of this model.

Another contribution of this work is the identification of the singular shapes, the shape of the base and the MP that leads to singularity in all configurations. A number of singular shapes, including the L-I, I=I, and P-C shapes have been identified with the parameterized model. To the author's knowledge, this is the first time that singular shapes are reported in literature.

In our work, two major performances, namely, dexterity and motion/force transmission indices, are considered in optimum design and further compared. It is seen that both indices indicate the identical singular shapes. On the other hand, optimal designs with the two indices are different. This suggests that the optimal criteria has to be selected based on the design problems and requirements.

Acknowledgments

References

[1] S.M. Varedi, H.M. Daniali, D.D. Ganji, Kinematics of an offset 3-UPU translational parallel manipulator by the homotopy continuation method, Nonlinear Anal. 10 (3) (2009) 1767–1774.

[2] M.L. Husty, Non-singular assembly mode change in 3-RPR-parallel manipulators, in: A. Kecskeméthy, A. Müller (Eds.), Computational Kinematics: Proceedings of the 5th International Workshop on Computational Kinematics, Springer Berlin Heidelberg, Berlin, Heidelberg, 2009, pp. 51–60.
[3] J. Angeles, C. Gosselin, The optimum kinematic design of a planar three-degree-of-freedom parallel manipulator, ASME J. Mech. Trans. Autom. Des. 110 (1988) 35–41.
[4] S. Staicu, Inverse dynamics of the 3-PRR planar parallel robot, Robot. Auton. Syst. 57 (5) (2009) 556–563.
[5] S. Zarkandi, Kinematics of a star-triangle planar parallel manipulator, J. Mech. Sci. Technol. 25 (1) (2011) 3223–3230.
[6] J.-P. Merlet, C.M. Gosselin, N. Mouly, Workspaces of planar parallel manipulators, Mech. Mach. Theory 33 (1) (1998) 7–20.
[7] I.A. Bonev, D. Zlatanov, C.M. Gosselin, Singularity analysis of 3-DOF planar parallel mechanisms via screw theory, J. Mech. Des. 125 (3) (2003) 573–581.
[8] F. Gao, X.-J. Liu, X. Chen, The relationships between the shapes of the workspaces and the link lengths of 3-DOF symmetrical planar parallel manipulators, Mech. Mach. Theory 36 (2) (2001) 205–220.
[9] C. Gwang-Jo, C. Kee-Bong, Development of nano order manipulation system based on 3-PPR planar parallel mechanism, in: 2004 IEEE International Conference on Robotics and Biomimetics, 2004, pp. 612–616.
[10] K.-B. Choi, Kinematic analysis and optimal design of 3-PPR planar parallel manipulator, KSME Int. J. 17 (4) (2003) 528–537.
[11] S. Bai, S. Caro, Design and analysis of a 3-PPR planar robot with U-shape base, in: 2009 International Conference on Advanced Robotics, 2009, pp. 1–6.
[12] G. Wu, S. Bai, J.A. Kepler, S. Caro, Error modeling and experimental validation of a planar 3-PPR parallel manipulator with joint clearances, J. Mech. Robot. 4 (4) (2012) 041008 (041001-041012).
[13] X. Wu, Z. Xie, D. Song, F. Liu, J. Luo, B. Mao, Forward kinematics of 3-PPR parallel mechanism based on improved ant colony algorithm, Trans. Chin. Soc. Agric. Mach. 46 (7) (2015) 339–344.
[14] Y. Singh, V. Vinoth, Y.R. Kiran, J.K. Mohanta, S. Mohan, Inverse dynamics and control of a 3-DOF planar parallel (U-shaped 3-PPR) manipulator, Robot. Comput.-Integr. Manuf. 34 (2015) 164–179.
[15] N. Binaud, S. Caro, S. Bai, P. Wenger, Comparison of 3-PPR parallel planar manipulators based on their sensitivity to joint clearances, in: 2010 IEEE/RSJ International Conference on Intelligent Robots and Systems, 2010, pp. 2778–2783.
[16] J.K. Salisbury, J.J. Craig, Articulated hands, Int. J. Robot. Res. 1 (1) (1982) 4–17.
[17] J. Wu, J. Wang, L. Wang, Z. You, Performance comparison of three planar 3-DOF parallel manipulators with 4-RRR, 3-RRR and 2-RRR structures, Mechatronics 20 (4) (2010) 510–517.
[18] S. Patel, T. Sobh, Manipulator performance measures - a comprehensive literature survey, J. Intell. Robot. Syst. 77 (3) (2015) 547–570.
[19] C. Gosselin, J. Angeles, A global performance index for the kinematic optimization of robotic manipulators, J. Mech. Des. 113 (3) (1991) 220–226.
[20] J. Wang, C. Wu, X.-J. Liu, Performance evaluation of parallel manipulators: Motion/force transmissibility and its index, Mech. Mach. Theory 45 (10) (2010) 1462–1476.
[21] C. Chen, J. Angeles, Generalized transmission index and transmission quality for spatial linkages, Mech. Mach. Theory 42 (9) (2007) 1225–1237.
[22] Y. Zhao, J. Wang, Y. Cao, B. Liang, T. Zhao, Constant motion/force transmission analysis and synthesis of a class of translational parallel mechanisms, Mech. Mach. Theory 108 (2017) 57–74.
[23] G. Wu, P. Zou, Comparison of 3-DOF asymmetrical spherical parallel manipulators with respect to motion/force transmission and stiffness, Mech. Mach. Theory 105 (2016) 369–387.